Received: 6 May 2024 | Revised: 14 August 2024 | Accepted: 19 August 2024

DOI: 10.1002/nbm.5254

RESEARCH ARTICLE

NMR IN BIOMEDICINE WILEY

Characterizing diffusion-controlled release of small-molecules using quantitative MRI in view of applications to orthopedic infection

Greg Hong [1,2,3] | Tina Khazaee [1,2,3] | Santiago F. Cobos [1,2,3] | Spencer D. Christiansen [1,3] | Junmin Liu [1] | Maria Drangova [1,2,3] | David W. Holdsworth [1,2,3]

[1]Imaging Research Laboratories, Robarts Research Institute, Western University, London, Ontario, Canada

[2]Bone and Joint Institute, Western University, London, Ontario, Canada

[3]Department of Medical Biophysics, Schulich School of Medicine & Dentistry, Western University, London, Ontario, Canada

Correspondence
David W. Holdsworth, Imaging Research Laboratories, Robarts Research Institute, Western University, London, Ontario, Canada.
Email: dholdsworth@robarts.ca

Funding information
Canadian Institutes of Health Research, Grant/Award Numbers: FDN 148474, PJT 159665; Ontario Research Fund, Grant/Award Number: RE-077-66; New Frontiers in Research Fund, Grant/Award Number: NFRFE-2019-00790; Transdisciplinary Bone & Joint Training Award from the Collaborative Training Program in Musculoskeletal Health Research at the University of Western Ontario; Centre for Functional and Metabolic Mapping Internal Funding Program and a Brain Canada Platform Support Grant

Abstract

Calcium sulfate is an established carrier for localized drug delivery, but a means to non-invasively measure drug release, which would improve our understanding of localized delivery, remains an unmet need. We aim to quantitatively estimate the diffusion-controlled release of small molecules loaded into a calcium sulfate carrier through a gadobutrol-based contrast agent, which acts as a surrogate small molecule. A central cylindrical core made of calcium sulfate, either alone or within a metal scaffold, is loaded with contrast agents that release into agar. Multi-echo scans are acquired at multiple time points over 4 weeks and processed into R2* and quantitative susceptibility mapping (QSM) maps. Mean R2* values are fit to a known drug delivery model, which are then compared with the decrease in core QSM. Fitting R2* measurements of calcium sulfate core while constraining constants to a drug release model results in an R^2-value of 0.991, yielding a diffusion constant of 4.59×10^{-11} m^2 s^{-1}. Incorporating the carrier within a metal scaffold results in a slower release. QSM shows the resulting loss of susceptibility in the non-metal core but is unreliable around metal. R2* characterizes the released gadobutrol, and QSM detects the resulting decrease in core susceptibility. The addition of a porous metal scaffold slows the release of gadobutrol, as expected.

KEYWORDS
antibiotics, calcium sulfate, drug delivery, infection, orthopedics

Abbreviations: GRE, gradient echo; MW, molecular weight; PETG, polyethylene terephthalate glycol; PJI, periprosthetic joint infection; PLA, polylactic acid; QSM, quantitative susceptibility mapping; ROI, regions of interest; SNR, signal-to-noise ratio; SoSPfC, sum of square of the points from the curve.

Maria Drangova and David W. Holdsworth represent equal contribution.

1 | INTRODUCTION

When developing a localized drug delivery system, the goals are to precisely target the cause of the disease and deliver the correct therapeutic concentration over an optimal time period.[1] To reach these goals, a carrier material, typically in the form of a simple matrix system,[2] hydrogels,[3,4] or targeted nanoparticles,[5,6] are incorporated with drugs and placed at the disease sites.[1] As a matrix-type carrier, calcium sulfate hemihydrate has a long history for the delivery of small molecules in a variety of applications, such as the delivery of antibiotics,[7,8] cancer-related drugs,[9] and other bioactive agents.[2] Being used as a bone filler[10] and bone graft substitute[11] in orthopedics, calcium sulfate has earned an excellent reputation for its biocompatibility and osteoconductive properties.[12] Currently, calcium sulfate is commonly used to deliver antibiotics to treat periprosthetic joint infection (PJI).[13,14] Infection is currently the leading cause of early revision of both hip and knee implants in North America[15,16] and is likely to grow more prevalent,[17] particularly as implant design improves fixation and mechanical stability.

Not only is it important to deliver antibiotics locally during therapy, but it is also desirable to characterize the pharmacokinetics of antibiotic release. Numerous in-vitro studies of drug diffusion from calcium sulfate antibiotic carriers via chemical analysis of eluants have been reported.[7,18] In-vivo studies examining antibiotic elution through surgical drains and serum have also been performed, but are limited by concerns over prolonged drain placement[7] and the lack of information about the dynamical diffusion process. These limitations contribute to the need for a means of non-invasive measurement of antibiotic release from calcium sulfate using imaging techniques, which would improve our understanding of localized antibiotic delivery in the treatment of PJI, particularly in vivo. Micro-CT has previously been proposed as a viable means of characterizing diffusion-controlled release of small molecules through the use of a contrast agent[19] loaded into a calcium sulfate matrix core releasing into a surrounding volume of agar over multiple time points. This proof of concept was demonstrated to be effective with micro-CT, but clinical application will be limited because of the risks associated with ionizing radiation if applied in vivo.

There are a few factors that indicate that MRI is a viable, non-invasive modality for imaging the diffusion-controlled release of small molecules, specifically gadobutrol contrast agents. The idea of using MRI to measure the diffusion of gadolinium-based contrast media is not new[20,21]; however, quantitative MRI has introduced new methods for this type of study. Critically, studies have shown that magnetic susceptibility is highly correlated to both gadolinium concentration[22] and CT-attenuation values[23]; it is also well known that gadolinium concentration is associated with R2*.[24] Molecular weight (MW) is known to be a dominant factor in small-molecule diffusion,[25] and gadolinium-based contrast agents are of similar MW to the antibiotics that are commonly deployed for orthopedic applications.

One prominent concern surrounding localized drug delivery, particularly in orthopedics, is that most carriers, including calcium sulfate, lack load-bearing capability.[26] Preliminary attempts to alleviate this concern include a study of the effects of deploying calcium sulfate within a simple reservoir built through resin 3D-printing[27]; however, a better solution may be found through metal 3D-printing. A recently proposed example of this is the use of 3D-printed porous metal implants, which have shown excellent mechanical suitability,[28–31] promising influence on bone ingrowth,[32] and clinical viability.[33] While 3D-printed porous metal implants have shown promise as a means of providing mechanical support and a stable environment for new bone formation, they still suffer some of the downsides of traditional metal implants, such as biological incompatibility, lack of osteoinductivity,[34] and potential for infection.[35] One promising solution to the latter problem (infection) is having the porous metal implants act as a scaffold that hosts an antibiotic carrier. For example, porous metal implants have also been used for loading drug-laden porous gelatin[36] and antibacterial hydrogels[37] by incorporating the carrier material into the implant's void spaces. Similarly, incorporating calcium sulfate into a porous implant would allow the metal structure to act as a scaffold that alleviates mechanical load from the carrier, which would allow the combined implant to elute antibiotics directly into the periprosthetic space instead of on the periphery of the infected joint. However, performing quantitative MRI around metals faces challenges associated with the susceptibility-induced field inhomogeneity that leads to artifacts in both magnitude and phase. Fortunately, it has been previously shown that highly porous 3D-printed metal scaffolds are MR compatible and exhibit decreased effective susceptibility proportional to their porosity,[38] and thus a highly porous scaffold filled with calcium sulfate may still be amenable to MRI-based measurements and eventual clinical monitoring.

The objective of this study is to quantitatively measure the release and diffusion of contrast agents loaded into calcium sulfate, both on its own and when contained within a porous metal scaffold. By using a clinically available gadobutrol-based contrast agent (Gadovist; MW = 604.7) with an MW similar to common antibiotic drugs (tobramycin; MW = 467.5 and gentamicin; MW = 477.6), we investigate the hypothesis that R2* and quantitative susceptibility mapping (QSM), derived from multi-echo gradient echo (GRE), can be used to characterize the diffusion-controlled release of small molecules over time.

2 | METHODS

2.1 | Experimental setup

The experimental setup consists of a central cylindrical core made of a carrier material that releases small molecules into surrounding agar contained in a plastic enclosure, creating a finite-source, finite-sink setup. A silicone-elastomer mold to form the core was created from a two-part negative

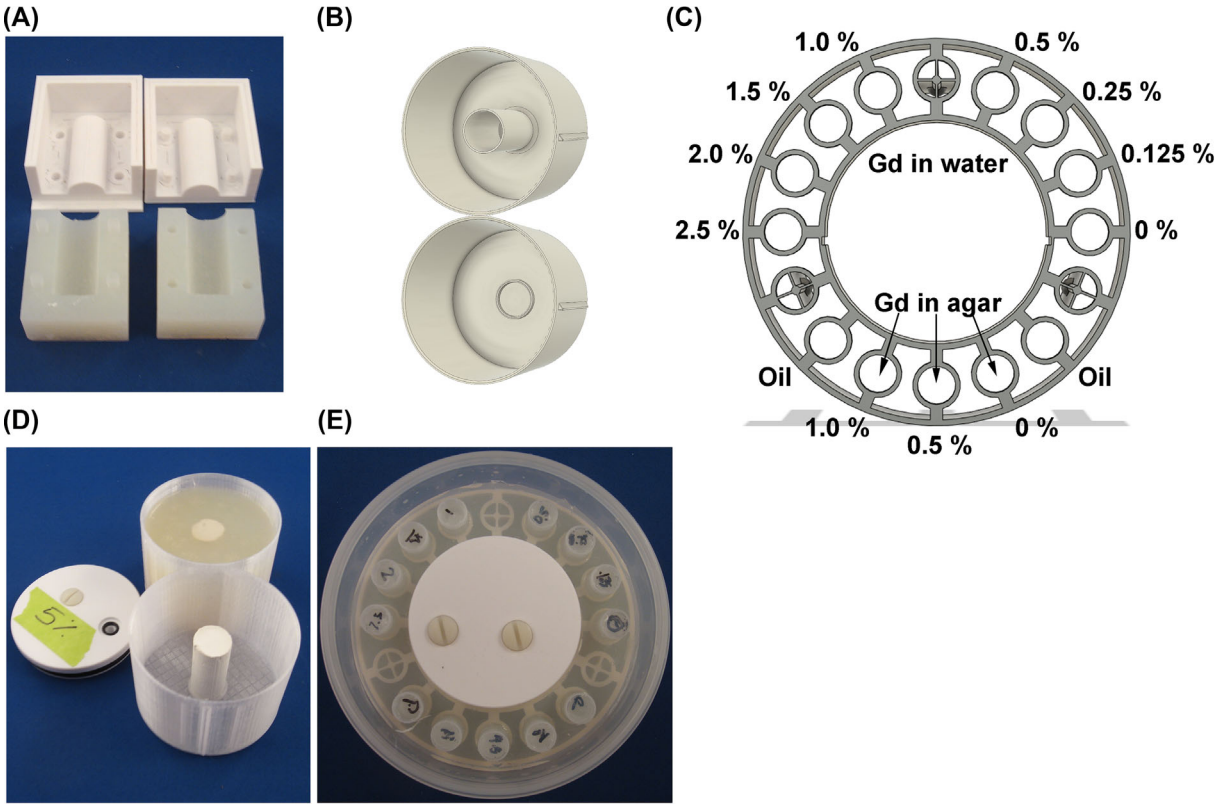

FIGURE 1 (A) Silicone mold made from 3D-printed polylactic acid (PLA) negatives. (B) Enclosures to hold central core (top: blocked diffusion, bottom: free diffusion). (C) Configuration of calibration vials and spherical markers used in registration. (D) Assembled sample (top: core surrounded by agar, bottom: core placed into inset prior to pouring agar). (E) Assembled phantom with calibration vials set in agar.

mold designed in Solidworks (Dassault Systèmes, Vélizy-Villacoublay, France) (Figure 1A) that was 3D-printed in polylactic acid (PLA). The mold was designed to form a cylinder of 17 mm radius and 40 mm length, which constitutes the central core. The enclosure, which contains both the core and its surrounding agar, has a diameter of 70 mm and either a raised inset to place the core (free diffusion experiment) or a 42 mm high wall that blocks the release of the molecules (Figure 1B). The "blocked" phantom was needed to separate the effect on R2* of the susceptibility-induced field inhomogeneity generated by the core and the effect of the increased concentration of the diffused molecules. The enclosures were 3D-printed by fused deposition on a Dremel 3D45 (Dremel, Mt. Prospect, Illinois) using clear polyethylene terephthalate glycol (PETG) for the diffusion experiment or white PLA for the blocked experiment. PETG was used for its mechanical properties, which allowed for a smaller raised inset, and PLA was used when a known small magnetic susceptibility (0.528 ppm shift)[39] was needed to minimize susceptibility effects.

2.2 | Sample preparation

Gadobutrol solution (50 mmol/L) was prepared by diluting Gadovist (Bayer Inc., Leverkusen, Germany) with distilled water at a 1:20 ratio. Calcium sulfate hemihydrate powder (Stimulan, Biocomposites Ltd., Keele, England) was mixed with 6 mL of the dilute Gadovist. The resulting paste was poured into the silicone mold and left to set, forming a cylindrical core. Agar gel was prepared by boiling 1 L of distilled water to remove dissolved gas, allowing it to cool to room temperature in a sealed container, and then mixing it with 35 g of agar and 80 mL of glycerol. The agar was heated to approximately 90°C and skimmed to remove impurities and air bubbles. The core was set into the enclosure, and the agar was poured when it was cooled to 60°C. The assembled samples were left to set for 3 h at room temperature prior to scanning. The samples were kept at room temperature between scans.

2.3 | Phantom design

An "external" annular phantom was also built to hold the assembled samples; this phantom served two purposes: holding a set of calibration vials and providing a set of fiducial markers needed to ascertain the phantom's precise orientation and center. Eight 2 mL calibration vials (Fisher Scientific, Waltham, Massachusetts) were prepared at 0.125%, 0.25%, 0.5%, 1%, 1.5%, 2%, and 2.5% of the raw (0.5 mmol/mL Gd) contrast agent

(Magnevist; Berlex Laboratories; Wayne, NJ) in distilled water, along with a vial of only distilled water.[40] Three additional vials were filled with agar made with 1.0%, 0.5%, and without Magnevist to assess the effect of agar on the quantitative images. Two vials of peanut oil were included to evaluate the effect of fat on our acquisition. The vials were held within a 3D-printed PLA construct; the configuration of these vials is shown in Figure 1C. The 3D-printed construct was also built with three 7-mm spherical markers used to determine the phantom's orientation relative to the coronal imaging plane. These markers were placed along a planar circle with a 51.45 mm radius. The assembled sample (Figure 1D; the enclosure holding the core and surrounding agar) snugly fitted into an inner ring, keeping the core consistently in the center of the ring formed by the markers; this enabled consistent repositioning of the assembled sample prior to each scan for phantom co-registration and alignment (see Section 2.7). The outer ring was designed to be placed within a 130-mm-diameter plastic container. The PLA construct, vials, and sample enclosure were placed in a plastic container and embedded in agar (Figure 1E).

2.4 | Gyroid-based porous metal core

A metal scaffold was designed based on a sheet-based gyroid—a triply periodic minimal surface that has been shown to have favorable mechanical properties for orthopedic applications, such as stiffness similar to bone and an appropriate strength for load-bearing implants.[28] The scaffold, whose effective susceptibility has been previously studied,[38] was designed with a porosity of 90% using Blender (Version 2.79, blender.org, Amsterdam, Netherlands), repeating a 6 mm^3 unit cell (Figure 2A) with a 0.2 mm wall thickness arranged into a $3 \times 3 \times 8$ array, which was then truncated into a cylinder matching the central core (Figure 2B). The resulting model was exported as stereolithography (STL) files and sliced for manufacture using the QuantAM build preparation software (Renishaw plc, Wotton-under-Edge, United Kingdom). The structures were 3D printed in Ti6Al4V medical grade titanium alloy (Ti6Al4V ELI-0406, Renishaw plc, United Kingdom, particle size 15–45 μm) using laser powder-bed fusion (AM400, Renishaw plc, Wotton-under-Edge, United Kingdom) at ADEISS (London, Canada) with a laser spot diameter of 70 μm and layer thickness of 40 μm. The manufactured porous titanium scaffold was loaded by filling the silicone mold with gadobutrol-loaded calcium sulfate and slowly inserting the metal core prior to setting, which allowed the fluid paste to fill the void spaces of the gyroid structure (Figure 2C).

2.5 | Imaging

Imaging was performed using a 3T Prisma scanner (Siemens Healthineers, Erlangen, Germany) with a Siemens 32-channel head coil at Western's Centre for Functional and Metabolic Mapping. A 3D multi-echo GRE sequence with echo times at 4.16, 5.52, 6.88, 8.26, 9.76, 11.67, 14.00, 16.34,[38] 18.67, and 21.00 ms (echo train length = 10) at 1 mm^3 resolution, with TR = 24 ms, 15° flip angle, BW = 1010 Hz/pixel, matrix size = 160 × 160 × 60, 16 cm FOV, and a total acquisition time of 3 min and 50 s, was acquired for processing into R2* and QSM images. The phantoms were scanned in the coronal configuration, with the samples perpendicular to B0. Scans were performed 3 and 10 h after pouring the agar, followed by scans at 32, 56, and 80 h, then at 1, 2, and 4 weeks. Phase and magnitude images were channel combined[41] and reconstructed on the scanner then exported as Digital Imaging and Communications in Medicine (DICOM) files. A smaller follow-up study was conducted to verify the compatibility of our methods with T1 mapping. This follow-up experiment used a Siemens product T1 mapping sequence (3D VIBE) with TR/TE = 5.68/2.03 ms, flip angle = 2 and 10°, and NEX = 2, scanned 20 h and 2 weeks after pouring.

2.6 | Quantitative mapping

Multi-echo complex data were assembled and processed from the scanner reconstructed magnitude and phase images using Matlab R2022b (Mathworks, Natick, Massachusetts) on a Mac Mini (2.8 GHz CPU and 16 GB RAM). Complex images were processed using the B0-NICE

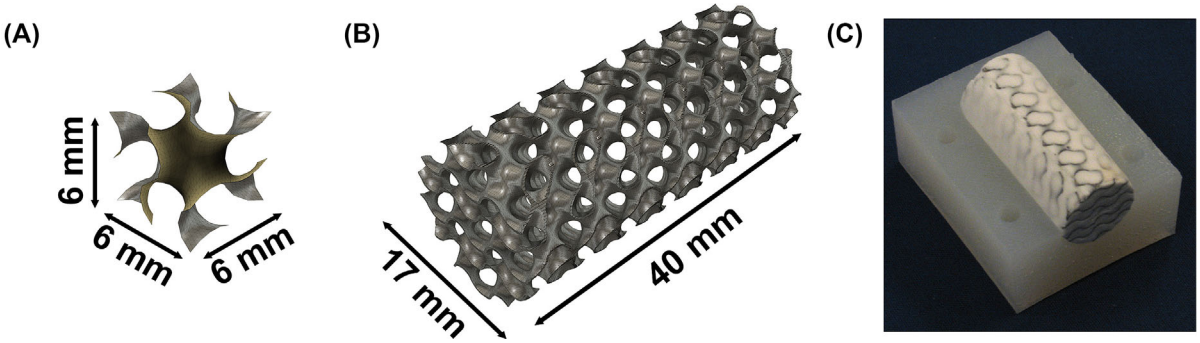

FIGURE 2 (A) Sheet-based gyroid unit cell. (B) Array of unit cells with 0.2 mm wall thickness truncated into cylinder. (C) Titanium 3D-printed scaffold filled with calcium sulfate.

algorithm[24,40,42] to generate fat fraction, R2*, and B0 maps from the 10 echoes. The R2* maps were calculated based on data-fitting of the magnitude images from the 10 echoes with echo spacing shortened (relative to previous B0-NICE applications) to reduce the effects of field inhomogeneity in the late echoes. QSM maps were generated using the MEDI algorithm[43] implemented on the 10-echo complex data and referenced to the values of the distilled-water vial. The QSM maps were used to measure the drop in core susceptibility as the contained gadobutrol was released into the surrounding agar.

2.7 | Phantom co-registration and alignment

Because imaging experiments over a prolonged period require sample repositioning, alignment of the images was required. The three alignment markers were identified in each image by thresholding, morphologically eroding the supporting structures, and calculating the markers' centroids. The center of the circle formed by the three markers indicates the precise coordinates of the center of the sample core. The markers also provide a measurement of both the in-plane rotation and through-plane tilt of the phantom within the magnet. Rotation matrices were calculated based on the marker centroids and used to co-align all images.

2.8 | Data analysis

The aligned magnitude images, R2*, and QSM maps were analyzed at each time point for both sample types (calcium sulfate only and calcium sulfate in metal) in both free diffusion and blocked enclosures. Calibration vial data were averaged within 8-mm circular regions of interest (ROI), 3-slices thick, centered on the plane defined by the markers. Similar regions were defined to calculate the average core susceptibility. Analysis of the diffusion samples was performed using radially averaged line profiles centered on the core, culminating in the quantification of gadobutrol release, as described below. The T1 maps were studied with methods similar to the R2* maps, with calibration vial data evaluated with ROIs and images analyzed with radially averaged line profiles centered on the core.

2.8.1 | Radial averaging

Radial averaging was employed to improve signal-to-noise ratio (SNR), minimize non-uniformities within the agar (e.g., small air bubbles), and simplify quantification and analysis while examining the slow diffusion of contrast agents through the agar. Radial averaging takes advantage of the radial symmetry of the sample and the radial nature of the diffusion of gadobutrol from the cylindrical core to average sample points that are equidistant to the core. In our case, where the images were aligned with the axis of the phantom, this was achieved by first averaging five slices, then creating and averaging 120 line profiles (spaced 3° apart) radiating from the center of the phantom. All data analysis was performed using Matlab.

2.8.2 | Gadobutrol release

The diffusion of small molecules can be modelled generally using Fick's laws of diffusion.[44] Our system (Gadovist in calcium sulfate formed into a cylinder) imitates a cylindrical diffusion-controlled (predominantly controlled by diffusional mass transport) drug delivery system, which has a known model.[44] The calcium sulfate core constitutes a "monolithic solution," as the molecule of interest is dispersed homogeneously throughout the calcium sulfate matrix, and thus the "drug" (Gadovist) release can be described by the approximation[44]:

$$\frac{M_t}{M_\infty} = 1 - \frac{4}{2.405^2}\exp\left(-\frac{2.405^2 Dt}{R^2}\right), \tag{1}$$

where M(t) is the cumulative amount of drug released at time t, M(∞) is the cumulative amount of drug released at infinity, D is the diffusion coefficient of the drug within the system, and R is the radius of the inner core cylinder. If R2* and concentration are linearly correlated, we can use the mean R2* value ($R2^*_{avg}(t)$) within the agar to measure the release of gadobutrol from the core into the enclosed agar through the ratio:

$$\frac{M_t}{M_\infty} = \frac{R2^*_{avg}(t) - R2^*_{avg}(0)}{R2^*_{avg}(\infty) - R2^*_{avg}(0)} \simeq \frac{R2^*_{avg}(t) - R2^*_{avg}(0)}{R2^*_{avg}(final) - R2^*_{avg}(0)} \tag{2}$$

with the approximation that $R2^*_{avg}(\infty)$ is equivalent to $R2^*_{avg}$(final), taken from the 4-week time point. For each time point, $R2^*_{avg}(t)$ was calculated by averaging the values with a 26-mm annulus encompassing the agar surrounding the 9-mm central core. A baseline $R2^*_{avg}(0)$ value was derived from the blocked (non-diffusing) phantom using the same averaging approach and subtracted from each $R2^*_{avg}(t)$. For the calcium sulfate-only core (non-metal), best-fit curves (exponential plateau) were calculated while constraining the constants (Equation 1—a molecule of interest is dispersed homogeneously throughout the matrix) to find the diffusion coefficient D of the system. The addition of an internal scaffold structure (metal core) invalidates the model of Equation (1), as the matrix is no longer continuous; however, a similar release curve can be expected. Therefore, the R2* data derived from the metal core phantom was fit to an exponential plateau but without the constants provided by the model. QSM measurements and R2*-based release curves are compared through an exponential decay fit of the core susceptibility.

2.8.3 | Statistical analysis

All line fitting was evaluated for quality of fit by the coefficient of determination (R^2 value) and the sum of square of the points from the curve (SoSPfC). All curve fitting and statistics were done in Prism 9 (version 9.0.0, GraphPad Software, San Diego, California).

3 | RESULTS

3.1 | Calcium sulfate core: quantitative maps

Representative aligned magnitude images (Figure 3A), R2* (Figure 3B), and QSM (Figure 3C) maps are shown at various time points over a 4-week period; the plane presented is 1 mm thick and orthogonal to the core. The magnitude images (Figure 3A) show the signal enhancement generated by the released, diffusing gadobutrol, where the radius of the high-signal circle increases over time. R2* images (Figure 3B) demonstrate a clear increase in R2* in the agar surrounding the central core, as expected. The QSM images (Figure 3C) show changes within the calcium sulfate core, where the core's magnetic susceptibility decreases as the high-susceptibility gadobutrol diffuses into the surrounding agar. Radially averaging the magnitude, R2*, and QSM images (Figure 4) provides further insight into the images. The averaged line profiles show that magnitude images do not change substantially beyond 7 days, suggesting that it takes a week for the initially released contrast agent to diffuse through the agar to the periphery of the sample. The R2* curves demonstrate a decreasing peak over time (<10 mm from the core) and an increasing concentration distal to the core (>20 mm from the center), which indicates that the total amount of gadobutrol leaving the core is decreasing and the total amount of gadobutrol in the agar is increasing.

3.2 | Calcium sulfate in a porous metal scaffold: quantitative maps

The porous metal scaffold was built with 92.56% porosity (measured by mass). The addition of metal has a clear effect on the first echo magnitude images (Figure 5A). The strong signal enhancement is still apparent, but the signal void surrounding the core has less defined edges, suggesting that the artifact stems from the metal structure. The field inhomogeneity induced by the titanium scaffold is apparent in R2* (Figure 5B); as a result, the volume adjacent to the core exhibits a fast-decaying signal (high R2*). The higher susceptibility of the core, compared with the calcium sulfate-only core, results in poorer quality QS maps. Nonetheless, a decrease in core susceptibility is seen over time (Figure 5C). The radially averaged line profiles confirm these observations, with a magnitude profile that is very similar to the non-metal experiment (compare Figure 6A to Figure 4A), a very high peak R2* (Figure 6B), and core susceptibility (Figure 6C) that are substantially higher than those without the metal scaffold. Note that, due to an error in acquisition, Week 2 data produced anomalously noisy maps, rendering them unsuitable for additional analysis.

3.3 | Calibration vials: relationship between concentration, magnitude, R2*, QSM, and T1

As expected, the relationship between magnitude and concentration was non-linear, and a linear relationship was observed between R2*, QSM, and gadobutrol concentration (Figure 7). Although it may be possible to describe the relationship between magnitude and concentration, the linear relationship between quantitative mapping and concentration provides an easy avenue for an experimental protocol that derives quantitative measurements of gadobutrol concentration that facilitates the calculation of total release and diffusion coefficient. As there are only four T1 scans, R1 (the reciprocal R1 is shown in order to compare with R2*) data for the water-based calibration vials are presented individually. R1 maps had large outliers (voxels with R1 > 1000), which were removed from the analysis. T1/R1 maps showed strong linearity and minimal noise at concentrations under 5 mM but poor performance at higher concentrations.

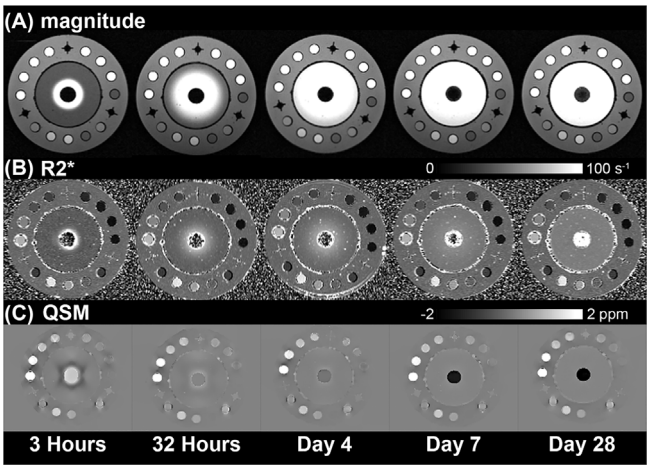

FIGURE 3 Time-series of magnitude, R2*, and quantitative susceptibility mapping (QSM) images at time points ranging from 3 h to 4 weeks. Slice shown is the plane of radial symmetry that bisects all three spherical markers. (A) Magnitude images of calcium sulfate (Stimulan) loaded with gadobutrol contrast agent (Gadovist). (B) R2* images calculated from signal decay over 10 echoes. (C) QSM map showing the core susceptibility decreasing as gadobutrol is released.

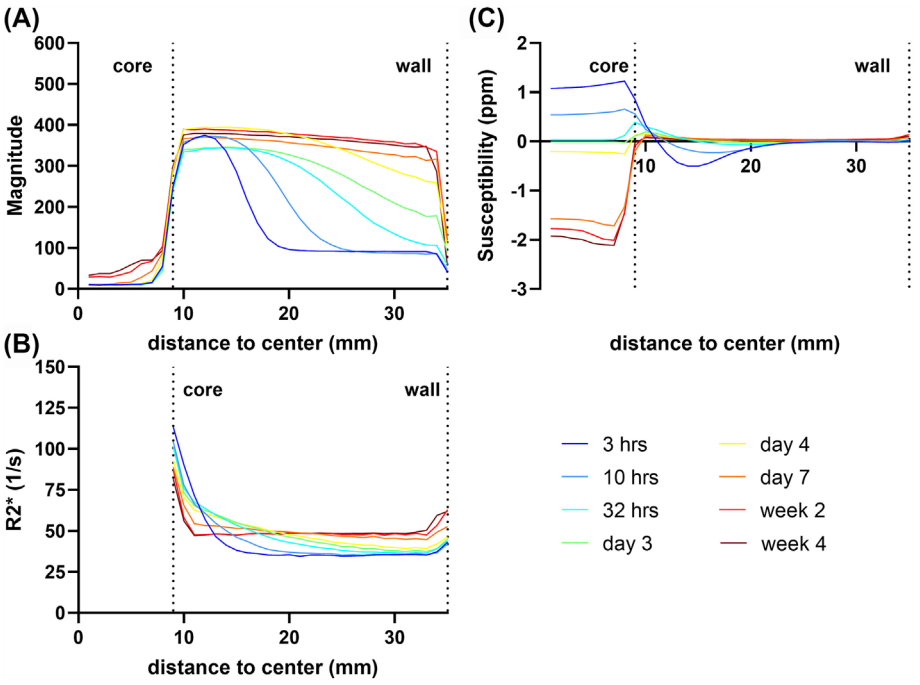

FIGURE 4 Radially averaged line profiles. Each data point averages 600 total samples, spanning five slices of 120 points spaced 3° apart. (A) Average intensity of magnitude images. (B) R2* line profiles. The lack of signal within the core resulted in a noisy fitting and is not shown. (C) Quantitative susceptibility mapping (QSM) line profiles. While the concentration of gadobutrol is not detectable within the agar, QSM is sensitive to the change in susceptibility of the core as gadobutrol is released.

3.4 | T1-mapping

The radially averaged line profiles and images are available in Figures S1 and S2, respectively, showing the results of a 2-timepoint experiment using T1 mapping. The magnitude and R2* images from this scan are similar to what was seen in the experiments described above, although the R1 maps surrounding the metal core are notably asymmetric. R1 line profiles show that measurements of T1 near the core and adjacent to the enclosure wall have problems, but T1 is otherwise a powerful tool for measuring gadobutrol concentration. In particular, T1 measurements are substantially less affected by the presence of metal than R2* and approach zero in the absence of contrast agents, which improves specificity.

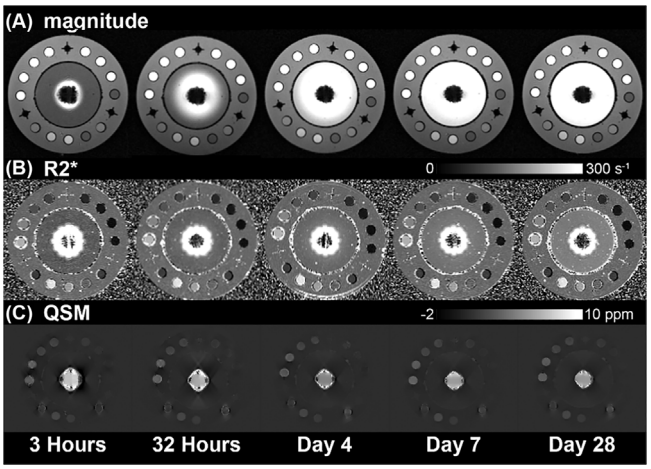

FIGURE 5 Time-series of magnitude, R2*, and quantitative susceptibility mapping (QSM) images at time points ranging from 3 h to 4 weeks of gadobutrol-loaded calcium sulfate in a porous metal scaffold. Slice shown is the plane of radial symmetry that bisects all three spherical markers. (A) Magnitude images of calcium sulfate (Stimulan) loaded with gadobutrol contrast agent (Gadovist) in a 3D-printed titanium-alloy porous scaffold. (B) R2* images calculated from signal decay over 10 echoes. R2* values near the core are heavily affected by field inhomogeneity. (C) QSM map showing the core susceptibility decreasing as gadobutrol is released. The higher susceptibility metal scaffold results in poor susceptibility estimates.

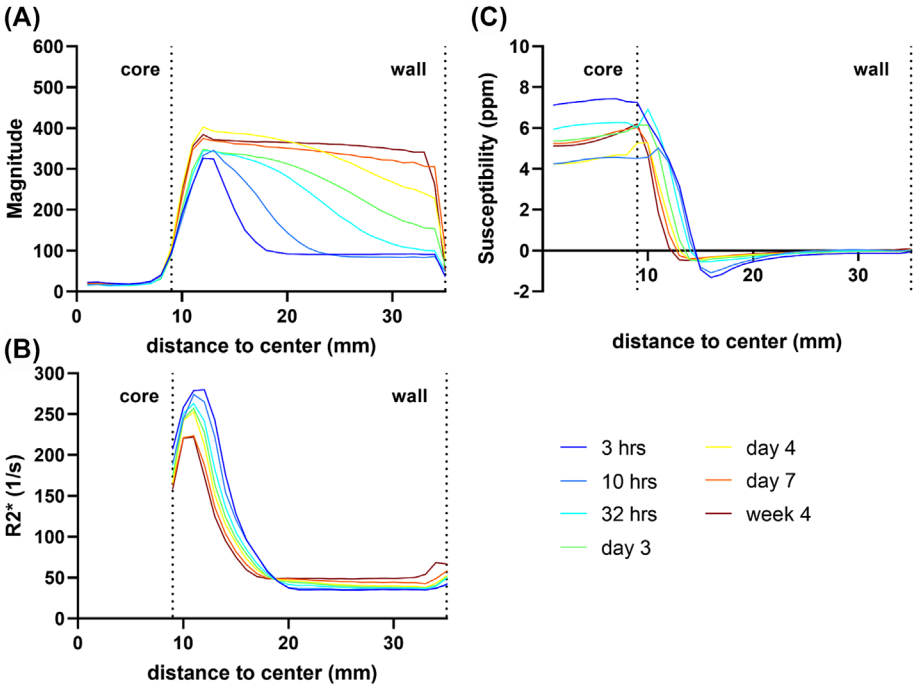

FIGURE 6 Radially averaged line profiles when a metal scaffold is added to the core. Each data point averages 600 total samples, spanning five slices of 120 points spaced 3° apart. (A) Average intensity of magnitude images. (B) R2* line profiles. The lack of signal within the core resulted in a noisy fitting and is not reliable. (C) quantitative susceptibility mapping (QSM) line profiles. The addition of metal to the calcium sulfate core increased susceptibility as expected but resulted in poor overall data quality.

3.5 | Release curves and diffusion coefficient

Analysis of the time-varying total concentration of gadobutrol in the agar (Equations 1 and 2) yields a set of R2* ratios governing the release of contrast agent out of the calcium sulfate into the agar. The baseline values of R2* at $t = 0$ (i.e., the time just before diffusion begins and no gadobutrol is present in the agar) were determined from the "blocked" (non-diffusing) phantom and were found to be 33.74 and 33.56 s^{-1} for the

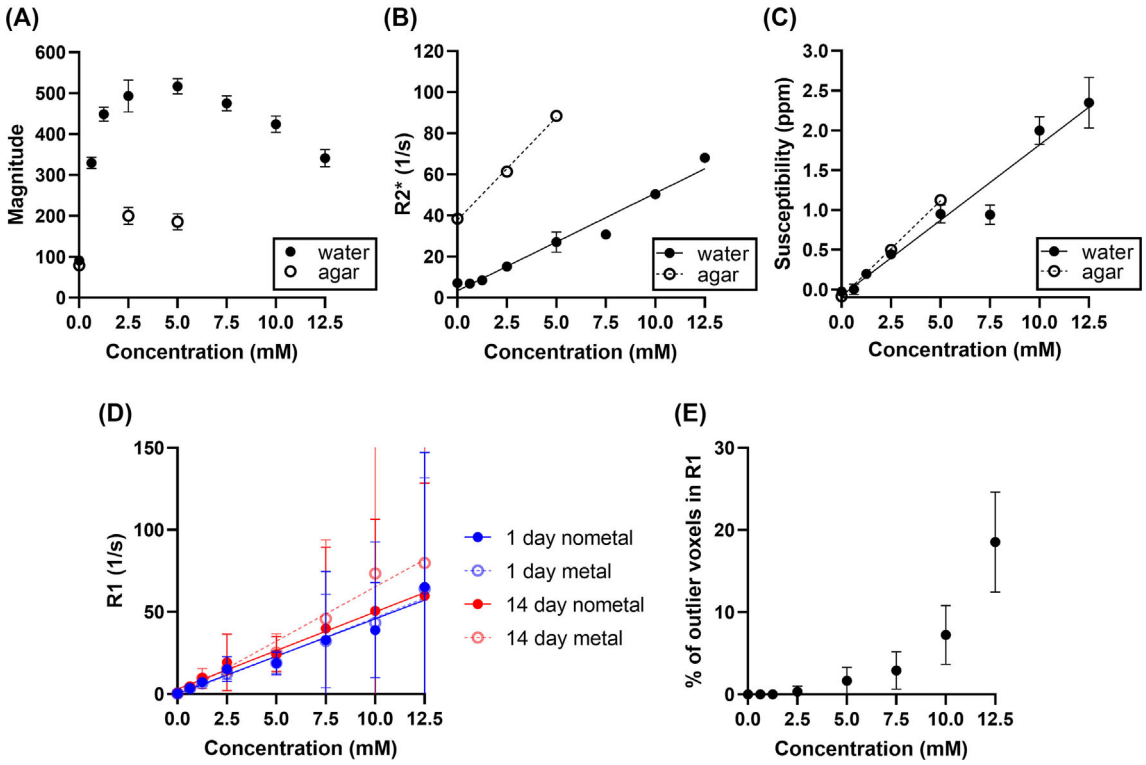

FIGURE 7 Volume average of three slices of each calibration vial (8 mm regions of interest [ROI]). (A) Magnitude; no correlation. (B) R2*; linear fit: water vials $R^2 = 0.956$, slope = 4.75 s^{-1}/mM; agar vials $R^2 = 0.995$, slope = 10 s^{-1}/mM. (C) quantitative susceptibility mapping (QSM); linear fit: water vials $R^2 = 0.938$, slope = 0.19 ppm/mM; agar vials $R^2 = 0.993$, slope = 0.24 ppm/mM. (D) Results of a separate T1 mapping experiment done 20 h and 14 days following pouring, showing R1 water vials for each scan; linear fit: $R^2 = 0.246–0.3102$, slope = 4.56–6.62 s^{-1}/M. (E) Percentage of voxels in ROI used in (D) that had value = 1000 s^{-1} and were removed as outliers.

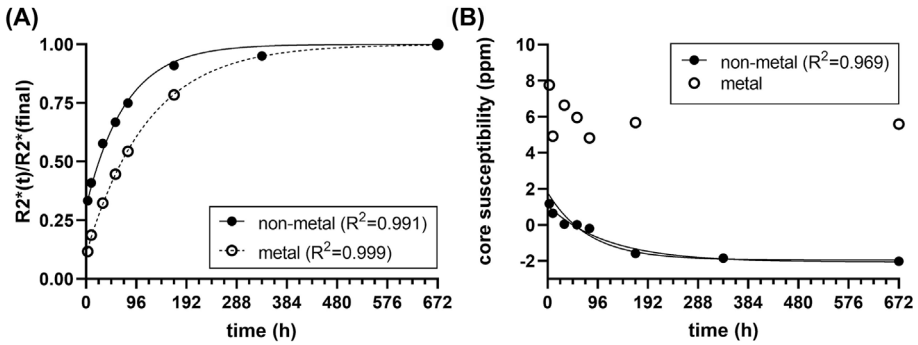

FIGURE 8 Diffusion curves measuring released contrast agent. (A) The ratio $R2^*_{avg}(t)/R2^*_{avg}(final)$ is used as a measurement of concentration(t)/concentration(∞), representing cumulative amounts of contrast agent in the agar. An outlier (metal, 2nd week) was excluded because of poor image quality. The non-metal release curve yields a diffusion constant of 4.59×10^{-11} m^2/s. (B) The susceptibility of the calcium sulfate core measured through quantitative susceptibility mapping (QSM). The addition of metal to the calcium sulfate core increased susceptibility as expected but resulted in poor overall data quality.

calcium sulfate-only (non-metal) and calcium sulfate-in-scaffold (metal) cores, respectively. Time-release curves were calculated by subtracting the baseline t = 0 R2* values from all corresponding average R2* values, representing released gadobutrol concentrations over time. The resulting release curve (Figure 8A, non-metal) has an R^2-value of 0.991 and an SoSPfC-value of 0.016, indicating that the data fits the theoretical model[44] well. The curve-fit results in a decay constant of 3.67×10^{-6} s^{-1}, yielding a diffusion constant of 4.59×10^{-11} m^2 s^{-1}. Fitting the core susceptibility values from the QSM images (Figure 8B, non-metal) yields an exponential decay with a decay constant of 2.4×10^{-6} s^{-1} (an R^2-value of 0.969 and an SoSPfC-value of 0.31). Although the addition of the Ti scaffold invalidates the mathematical model, the release curve exhibits a

similar exponential plateau (Figure 8A, metal) with a decay constant of 2.37×10^{-6} s^{-1}, an R^2-value of 0.999, and an SoSPfC-value of 0.004 (the improved fit is due to not constraining the curve to the drug release model). As expected, when adding titanium to the core, QSM does show an increase in susceptibility (Figure 8B, metal); unfortunately, the susceptibility changes over time did not fit the expected exponential decay.

4 | DISCUSSION

In this work, we have demonstrated that quantitative MRI can monitor the diffusion-controlled release of a gadobutrol contrast agent. As MW plays a dominant role in governing small-molecule diffusion, it is ideal if the contrast agent's MW is similar to the MW of the antibiotics it is intended to simulate. The specific contrast agent employed in this study, Gadovist (MW = 604.7, freely soluble in water), is reasonably similar to two antibiotics that are often mixed with Stimulan, tobramycin (MW = 467.5, freely soluble in water) and gentamicin (MW = 477.6, freely soluble in water), making it an appropriate choice for potential clinical applications.

4.1 | Calcium sulfate-only core

As expected, the gadobutrol that is released from the calcium sulfate core has a signal-enhancing effect, with a high-signal circle increasing in radius over time as the contrast agent slowly diffuses through the agar. A radially symmetric plane was identified and used for radial averaging and modelling diffusion-controlled release. We have shown that R2* is sensitive to small changes in gadobutrol concentration and that those changes can be used as a measure of concentration for modelling release kinetics. The released gadobutrol also resulted in a decrease in magnetic susceptibility of the central core that is detectable by QSM; this decrease in core susceptibility (from paramagnetic to diamagnetic relative to water) is consistent with the diamagnetic nature of calcium sulfate.[45] Note that the diamagnetic nature of non-contrast enhanced calcium sulfate is useful for offsetting some of the magnetic susceptibility increase introduced by the addition of gadobutrol. The decay constant found by QSM, while comparable to that found with R2*, was 34% lower; we suspect that in the early time points, the high concentration of gadobutrol in the agar directly adjacent to the core decreased the susceptibility difference between the core and agar, resulting in a lower measured core QSM.

Calcium sulfate, in the form of Stimulan, is clinically used as an antibiotic carrier, typically as 6-mm beads implanted at the surgical site. A clinical study that measured drained serum antibiotic concentrations daily for 5 days post-surgery demonstrated a release profile where antibiotic concentration peaked on Day 1 and decreased day to day,[7] following a curve with a similar shape to that found in our experiments. A study examining the diffusion of a different small molecule (platinum) using calcium sulfate beads in agar through a series of concentric cubic shells found an overall decrease in concentration in the innermost shells and an overall increase in concentration in the outermost shells,[9] which is in line with what we see in our R2* line profiles over time. Using mean R2* values as a surrogate for the cumulative release of gadobutrol in a diffusion-controlled release model demonstrated an excellent fit that provided an accurate estimate of the diffusion coefficient (D) for this system. Comparative values of D for gadobutrol from calcium sulfate have not been previously reported, and the diffusion coefficient will depend strongly on the properties of the material through which it is diffusing, so comparison to the literature may be difficult to interpret. However, a CT study conducted using the same experimental design (contrast agent loaded into a cylindrical core surrounded by agar)[19] found a diffusion coefficient for iohexol in calcium sulfate (4.6×10^{-11} m^2 s^{-1}) that is similar to the value for gadobutrol diffusion reported in our study (4.59×10^{-11} m^2 s^{-1}).

4.2 | Calcium sulfate contained in a porous metal scaffold

Calcium sulfate is commonly used as an antibiotic carrier without a supporting structure; the use of a porous metal scaffold would enhance the mechanical properties. It has been shown in animal experiments[37] that integrating a carrier into a load-bearing scaffold maintains its antibacterial capability, promising better drug delivery than the current practice of packing the surgery site with antibiotic calcium sulfate beads[13] by virtue of direct contact with the infection site. Incorporating a drug-laden carrier into a porous metal scaffold emulates the drug-delivery function of an antibiotic-loaded temporary spacer,[46] ideally while improving mechanical stability sufficiently to employ as a permanent implant. However, magnetic susceptibility effects become a potential concern when incorporating the calcium sulfate carrier into a porous metal scaffold. For this reason, one component of our study evaluated the possibility of quantitative characterization of gadobutrol release from calcium sulfate in the presence of a titanium scaffold. It is apparent from the study that the gadobutrol-induced signal enhancement effect is still evident surrounding the metal core. Unfortunately, the increased magnetic susceptibility makes QSM unreliable, which is likely due to multiple materials with very different susceptibilities existing in a single voxel, causing significant B0 variation within that voxel and also significant transverse relaxation, making it difficult to fit the phase evolution, particularly at later echo times. The increased susceptibility (and resulting field inhomogeneity) also affected R2* in the volume adjacent to the core; however, we present evidence that R2* is still sensitive to concentration changes when examining volumes distal to the core. Calculating a release curve in a similar manner to the calcium sulfate-only core (without the constants supplied by the model as the

model is limited to uniform geometry) shows that the addition of the scaffold impedes the release of gadobutrol, resulting in a slower initial surge and slowed overall release that eventually results in a similar cumulative concentration (by Week 4). Further work is needed to reliably employ quantitative imaging around calcium sulfate-loaded porous metal scaffolds, but this preliminary work demonstrates both its feasibility and potential value for studying the effects of carrier modifications on drug release using non-invasive measurements.

4.3 | Clinical potential

The imaging methods described in this study are likely to be clinically translatable. The multi-echo GRE employed for quantitative mapping is a product sequence, and the processing algorithm has been previously used for in vivo studies.[40,42] The B0-NICE algorithm[24,40,42] has the ability to measure fat fraction simultaneously with R2* and QSM; although this capability was not used in this study, it will be useful when fat-suppressed images, which are typical in orthopedic MRI,[47] are requested. We also conducted experiments showing the viability of the more commonly used T1 mapping in this application. Aside from the fact that R2* and QSM can be processed from the same scan, our experiments with T1 mapping showed two disadvantages compared with R2*—inaccurate measurements at higher concentrations and a small but noticeable asymmetry in the images surrounding metal. Another concerning element is that noisy voxels in R1 maps often have very large values; although they are easily filtered and discarded as outliers, they still present a concern for calculating release curves. T1 mapping does have advantages as well; radially averaged line profiles indicate that T1 is less affected by field inhomogeneity effects than R2*, particularly surrounding the metal core, and R1 goes to zero as contrast agent concentration decreases. The concerns surrounding T1 mapping, particularly regarding high concentrations of contrast agent, are unlikely to be relevant with the smaller calcium sulfate beads used clinically, as we would expect lower concentrations surrounding a smaller carrier.

The dearth of existing means to track antibiotic delivery should also promote clinical translation; existing methods of monitoring antibiotic delivery in patients require examination of surgical drains and serum, leading to concerns about prolonged drain placement.[7] These existing methods are also limited in their ability to gather information about the diffusion and clearance processes; MR imaging may be able to help us better understand how small molecules are cleared in vivo as the contrast agent can be detected even with simple magnitude images. Clinical applications of Stimulan deploy numerous small hemispheric beads,[13] which should make QSM more effective as they are closer to what the algorithm was designed for—being smaller and more spherical. These beads are also bio-absorbable, and resorption has been reported to occur within 6 weeks.[14] Recent research in QSM source separation methods[48–51] may help monitor the resorption of the bio-absorbable beads by separating the overall susceptibility of the bead to its constituent contributions from the diamagnetic (calcium sulfate) and paramagnetic (gadobutrol) sources.

Incorporating the calcium sulfate carrier into a porous metal scaffold, while more challenging to analyze, is likely to resemble the eventual in vivo implant relatively closely, likely resulting in more direct in vitro-to-in vivo translation. Furthermore, the diffusion of contrast agents directly into the periprosthetic space will likely prove valuable even with traditional qualitative MRI; it increases the signal surrounding the implant, which, combined with the low effective susceptibility of the porous implant, could allow for reliable anatomical information to be scanned very close to the prosthesis.

This manuscript has demonstrated the principle of quantitatively monitoring the diffusion of small molecules from a Ti-based scaffold impregnated with calcium sulfate. However, the technique is applicable broadly to all MR-compatible scaffolds, including recently described 3D-printed porous iron–manganese scaffolds.[52]

4.4 | Limitations

This study is limited in scope and intended primarily to disseminate a novel potential application of gadobutrol-based contrast agents as a surrogate small molecule, which would be used to enable MRI as a non-invasive means of estimating drug release. Our study design aimed to demonstrate that the release of gadobutrol from a carrier follows a known drug release model in a tightly controlled environment. This experimental setup, although useful for validation, has limitations; these limitations include differences in geometry versus clinical application, our limited exploration of alternative pulse sequences, and limitations of the drug release model.

4.4.1 | Geometry-related limitations

This study is limited to a specific, tightly controlled setup that limits its predictive utility in more clinically realistic applications. We employed a cylindrical shape in this study as it is both useful for modelling and curve fitting, and the size of the metal scaffold is a reasonable approximation of its potential use as an implant. However, clinical applications of Stimulan commonly deploy numerous small hemispheric beads, which is not

amenable to the same analysis.[13] Although the smaller beads would have the benefit of decreasing susceptibility-related field inhomogeneity, it is difficult to compare our findings using a relatively large cylinder with the experiments studying the clinically used beads.

4.4.2 | Imaging-related limitations

The scope of this study did not include a comparison of different imaging sequences or quantitative parameters, as the purpose was to demonstrate that it is possible to use MRI to characterize the diffusion-controlled release of small molecules over time. We thus elected to run our experiments with a sequence that could simultaneously measure the concentration of gadobutrol inside the core (QSM) and within the agar (R2*). We conducted additional experiments to verify that T1 mapping could also be an effective tool for measuring gadobutrol concentration and found that, compared with R2*, T1 is limited in the range of concentrations that can be measured accurately. However, our experiments also show that this disadvantage may not be relevant in practice, as the concentrations being measured in our proposed application are small. T1 should be an effective tool for measuring the diffusion-controlled release of contrast agents, particularly in the presence of metal. Changes in T1 are also more specific to changes in concentration, which is likely to be valuable when making in vivo measurements.

Our study was performed at 3T, which is typical for clinical MRI, particularly for orthopedics. It is well known that susceptibility artifacts scale directly with field strength, with R2* being particularly affected. At higher field strengths, such as those used in pre-clinical imaging, it may be pertinent to employ T1 imaging or QSM as the primary measurement for determining contrast agent release.

There are also limitations of MRI relative to CT, such as the longer scan time, cost, and risk of gadolinium deposits. Although CT may be a better means of conducting this specific experiment, as it is easier to interpret and more specific in this well-controlled environment, it remains to be determined if the wide range of quantitative measurements available to MRI (many of which we have not explored in this study, such as chemical exchange saturation transfer[53]) will justify its cost and scan time. The risk associated with gadolinium deposition stemming from use as a surrogate drug-release measurement is also relatively minor, as the initial concentration of contrast agent in the matrix is only 5% and is released slowly. Furthermore, CT contrast agents are also not risk-free[54,55]; thus, even if CT may be a better first option for monitoring drug release through a contrast agent surrogate, an alternative modality would still be valuable.

4.4.3 | Model-related limitations

We validated our results by fitting them to a drug release model[44] that solves Fick's laws of diffusion for a system analogous to our setup, consisting of a drug surrogate (the contrast agent) homogenously distributed in a matrix (calcium sulfate) with cylindrical geometry. The diffusion coefficient found in this experiment is not intended to predict behavior in vivo (where tissue perfusion and blood flow will complicate the analysis), but rather to show that this technique can characterize the diffusion-dominated release of small molecules in a tissue-mimicking medium.

4.4.4 | Application-related limitations

Although we have taken care to choose a contrast agent that is of similar MW to some clinically relevant antibiotics, this study does not attempt to verify that the surrogate molecule diffuses similarly to antibiotics. We assume that the surrogate molecules (gadobutrol) will diffuse through tissue in a way that is similar to similar-weight antibiotics (such as tobramycin or gentamicin); this is consistent with Fickian diffusion and the Stokes–Einstein equation.[25] In future studies, this approximation can be verified by adding gadobutrol to experiments described by Laycock et al.[8] for testing antibiotic activity. Specifically, we can verify the validity of our assumption that gadobutrol will diffuse similarly to antibiotics by loading both into a calcium sulfate bead (as used clinically), placing the bead in an agar plate, and examining zones of inhibition.

5 | CONCLUSION

We proposed a method for measuring the release of a gadobutrol-based contrast agent loaded into a calcium sulfate carrier using MRI. Results from quantitative imaging show that R2* and QSM are linearly proportional to gadobutrol concentration, agree with previously published studies, and fit a mathematical model of drug release. We also explored the effect of filling a highly porous metal scaffold with the gadobutrol-loaded carrier and found that, while further work is needed, quantitative imaging is still viable in spite of the increased core susceptibility. Overall, we have demonstrated the feasibility of MRI as a non-invasive means of characterizing the diffusion-controlled release of small molecules from a clinically relevant carrier through a contrast agent surrogate.

AUTHOR CONTRIBUTIONS

Greg Hong's (primary author) contribution to this work includes phantom design, fabrication and preparation, sample preparation, MR imaging and data collection, generating simulated field maps, co-registration between simulated and scanned images, data analysis, and manuscript preparation. Study conception and design were adapted for MRI from Tina Khazaee's work in CT. Spencer D. Christiansen assisted in adapting the MRI sequence and data processing created by Junmin Liu for this project. Santiago F. Cobos and Tina Khazaee conceived the use of sheet-gyroid unit cells for porous metal scaffolds. Junmin Liu, Maria Drangova, and David W. Holdsworth contributed to the data analysis and manuscript preparation.

ACKNOWLEDGMENTS

The authors acknowledge funding from the Canadian Institutes of Health Research (FDN 148474, PJT 159665), the Ontario Research Fund (RE-077-66), and the New Frontiers in Research Fund (NFRFE-2019-00790). G.H., T.K., and S.C. are supported in part by a Transdisciplinary Bone & Joint Training Award from the Collaborative Training Program in Musculoskeletal Health Research at the University of Western Ontario. Imaging for this project was performed at Western's Centre for sFunctional and Metabolic Mapping with funding from the Centre for Functional and Metabolic Mapping Internal Funding Program and a Brain Canada Platform Support Grant. The authors would also like to thank Tom Chmiel at ADEISS for his assistance with the manufacturing of the porous titanium scaffold.

CONFLICT OF INTEREST STATEMENT

The authors declare that they have no known competing financial interests or personal relationships that could have appeared to influence the work reported in this paper.

CODE AND DATA AVAILABILITY STATEMENT

The Matlab code and MRI data are available on Zenodo (10.5281/zenodo.7344615).

REFERENCES

1. Tibbitt MW, Dahlman JE, Langer R. Emerging frontiers in drug delivery. *J Am Chem Soc*. 2016;138(3):704-717. doi:10.1021/jacs.5b09974
2. Orellana BR, Hilt JZ, Puleo DA. Drug release from calcium sulfate-based composites. *J Biomed Mater Res B Appl Biomater*. 2015;103(1):135-142. doi:10.1002/jbm.b.33181
3. Narayanaswamy R, Torchilin VP. Hydrogels and their applications in targeted drug delivery. *Molecules*. 2019;24(3):603. doi:10.3390/molecules24030603
4. Sun Z, Song C, Wang C, Hu Y, Wu J. Hydrogel-based controlled drug delivery for cancer treatment: a review. *Mol Pharm*. 2020;17(2):373-391. doi:10.1021/acs.molpharmaceut.9b01020
5. Mitchell MJ, Billingsley MM, Haley RM, Wechsler ME, Peppas NA, Langer R. Engineering precision nanoparticles for drug delivery. *Nat Rev Drug Discov*. 2021;20(2):101-124. doi:10.1038/s41573-020-0090-8
6. Nikezić AVV, Bondžić AM, Vasić VM. Drug delivery systems based on nanoparticles and related nanostructures. *Eur J Pharm Sci*. 2020;151:105412. doi:10.1016/j.ejps.2020.105412
7. Maale GE, Eager JJ, Mohammadi DK, Calderon FA 2nd. Elution profiles of synthetic $CaSO_4$ hemihydrate beads loaded with vancomycin and tobramycin. *Eur J Drug Metab Pharmacokinet*. 2020;45(4):547-555. doi:10.1007/s13318-020-00622-8
8. Laycock PA, Cooper JJ, Howlin RP, Delury C, Aiken S, Stoodley P. In vitro efficacy of antibiotics released from calcium sulfate bone void filler beads. *Materials (Basel)*. 2018;11(11):2265. doi:10.3390/ma11112265
9. Phillips H, Maxwell EA, Schaeffer DJ, Fan TM. Simulation of spatial diffusion of platinum from carboplatin-impregnated calcium sulfate hemihydrate beads by use of an agarose gelatin tissue phantom. *Am J Vet Res*. 2018;79(6):592-599. doi:10.2460/ajvr.79.6.592
10. Thomas MV, Puleo DA. Calcium sulfate: properties and clinical applications. *J Biomed Mater Res B Appl Biomater*. 2009;88(2):597-610. doi:10.1002/jbm.b.31269
11. Moore WR, Graves SE, Bain GI. Synthetic bone graft substitutes. *ANZ J Surg*. 2001;71(6):354-361. doi:10.1046/j.1440-1622.2001.02128.x
12. Ene R, Nica M, Ene D, Cursaru A, Cirstoiu C. Review of calcium-sulphate-based ceramics and synthetic bone substitutes used for antibiotic delivery in PJI and osteomyelitis treatment. *EFORT Open Rev*. 2021;6(5):297-304. doi:10.1302/2058-5241.6.200083
13. Abosala A, Ali M. The use of calcium sulphate beads in periprosthetic joint infection, a systematic review. *J Bone Jt Infect*. 2020;5(1):43-49. doi:10.7150/jbji.41743
14. Lum ZC, Pereira GC. Local bio-absorbable antibiotic delivery in calcium sulfate beads in hip and knee arthroplasty. *J Orthop*. 2018;15(2):676-678. doi:10.1016/j.jor.2018.05.001
15. Canadian Institute for Health Information. *Hip and Knee Replacements in Canada, 2017–2018: Canadian Joint Replacement Registry Annual Report*. CIHI; 2019.
16. American Academy of Orthopaedic Surgeons. *American Joint Replacement Registry Annual Report 2019*. AAoS; 2019.
17. Schwartz AM, Farley KX, Guild GN, Bradbury TL Jr. Projections and epidemiology of revision hip and knee arthroplasty in the United States to 2030. *J Arthroplasty*. 2020;35(6):S79-S85. doi:10.1016/j.arth.2020.02.030
18. Moore K, Os RWV, Dusane DH, et al. Elution kinetics from antibiotic-loaded calcium sulfate beads, antibiotic-loaded polymethacrylate spacers, and a powdered antibiotic bolus for surgical site infections in a novel in vitro draining knee model. *Antibiotics (Basel)*. 2021;10(3):270. doi:10.3390/antibiotics10030270

19. Khazaee T, Norley CJ, Nikolov H, Pollmann S, Holdsworth D. *Micro-CT imaging technique to characterize diffusion of small-molecules*. Vol. 11317 MI. SPIE; 2020.
20. Gordon MJ, Chu KC, Margaritis A, Martin AJ, Ethier CR, Rutt BK. Measurement of Gd-DTPA diffusion through PVA hydrogel using a novel magnetic resonance imaging method. *Biotechnol Bioeng*. 1999;65(4):459-467. doi:10.1002/(SICI)1097-0290(19991120)65:43.0.CO;2-O
21. Penkova A, Rattanakijsuntorn K, Sadhal SS, et al. A technique for drug surrogate diffusion coefficient measurement by intravitreal injection. *Int J Heat Mass Transf*. 2014;70:504-514. doi:10.1016/j.ijheatmasstransfer.2013.11.002
22. Olsson E, Wirestam R, Lind E. MRI-based quantification of magnetic susceptibility in gel phantoms: assessment of measurement and calculation accuracy. *Radiol Res Pract*. 2018;2018:6709525. doi:10.1155/2018/6709525
23. Oshima S, Fushimi Y, Okada T, et al. Brain MRI with quantitative susceptibility mapping: relationship to CT attenuation values. *Radiology*. 2020;294(3):600-609. doi:10.1148/radiol.2019182934
24. Christiansen SD, Liu J, Boffa MB, Drangova M. Simultaneous R(2(*)) and quantitative susceptibility mapping measurement enables differentiation of thrombus hematocrit and age: an in vitro study at 3 T. *J Neurointerv Surg*. 2019;11(11):1155-1161. doi:10.1136/neurintsurg-2019-014802
25. Valencia D, González F. Understanding the linear correlation between diffusion coefficient and molecular weight. A model to estimate diffusion coefficients in acetonitrile solutions. *Electrochem Commun*. 2011;13(2):129-132. doi:10.1016/j.elecom.2010.11.032
26. Cavelier S, Tanzer M, Barthelat F. Maximizing the strength of calcium sulfate for structural bone grafts. *J Biomed Mater Res A*. 2020;108(4):963-971. doi:10.1002/jbm.a.36873
27. Allen B, Moore C, Seyler T, Gall K. Modulating antibiotic release from reservoirs in 3D-printed orthopedic devices to treat periprosthetic joint infection. *J Orthop Res*. 2020;38(10):2239-2249. doi:10.1002/jor.24640
28. Kelly CN, Francovich J, Julmi S, et al. Fatigue behavior of As-built selective laser melted titanium scaffolds with sheet-based gyroid microarchitecture for bone tissue engineering. *Acta Biomater*. 2019;94:610-626. doi:10.1016/j.actbio.2019.05.046
29. Zaharin HA, Abdul Rani AM, Azam FI, et al. Effect of unit cell type and pore size on porosity and mechanical behavior of additively manufactured Ti6Al4V scaffolds. *Materials (Basel)*. 2018;11(12):2402. doi:10.3390/ma11122402
30. Hitchon S, Anderson W, Milner JS, et al. Static compression and fatigue behavior of heat-treated selective laser melted titanium alloy (Ti6Al4V) gyroid cylinders. *J Mech Behav Miomed Mater*. 2023;146:106076. doi:10.1016/j.jmbbm.2023.106076
31. Hitchon S, Soltanmohammadi P, Milner J, Holdsworth D, Willing R. Porous versus solid shoulder implants in humeri of different bone densities: a finite element analysis. *J Orthop Res*. 2024;42(9):1897-1906. doi:10.1002/jor.25840
32. Cheong VS, Fromme P, Coathup MJ, Mumith A, Blunn GW. Partial bone formation in additive manufactured porous implants reduces predicted stress and danger of fatigue failure. *Ann Biomed Eng*. 2020;48(1):502-514. doi:10.1007/s10439-019-02369-z
33. Burastero G, Cavagnaro L, Chiarlone F, et al. Clinical study of outcomes after revision surgery using porous titanium custom-made implants for severe acetabular septic bone defects. *Int Orthop*. 2020;44(10):1957-1964. doi:10.1007/s00264-020-04623-9
34. Gu Y, Sun Y, Shujaat S, Braem A, Politis C, Jacobs R. 3D-printed porous Ti6Al4V scaffolds for long bone repair in animal models: a systematic review. *J Orthop Surg Res*. 2022;17(1):68. doi:10.1186/s13018-022-02960-6
35. Dubey A, Vahabi H, Kumaravel V. Antimicrobial and biodegradable 3D printed scaffolds for orthopedic infections. *ACS Biomater Sci Eng*. 2023;9(7):4020-4044. doi:10.1021/acsbiomaterials.3c00115
36. Cai B, Huang L, Wang J, et al. 3D printed multifunctional Ti(6)Al(4)V-based hybrid scaffold for the management of osteosarcoma. *Bioconjug Chem*. 2021;32(10):2184-2194. doi:10.1021/acs.bioconjchem.1c00367
37. Qiao S, Wu D, Li Z, et al. The combination of multi-functional ingredients-loaded hydrogels and three-dimensional printed porous titanium alloys for infective bone defect treatment. *J Tissue Eng*. 2020;11:2041731420965797. doi:10.1177/2041731420965797
38. Hong G, Liu J, Cobos SF, Khazaee T, Drangova M, Holdsworth DW. Effective magnetic susceptibility of 3D-printed porous metal scaffolds. *Magn Reson Med*. 2022;87(6):2947-2956. doi:10.1002/mrm.29136
39. Wapler MC, Leupold J, Dragonu I, von Elverfeld D, Zaitsev M, Wallrabe U. Magnetic properties of materials for MR engineering, micro-MR and beyond. *J Magn Reson*. 2014;242:233-242. doi:10.1016/j.jmr.2014.02.005
40. Liu J, Christiansen SD, Drangova M. Single multi-echo GRE acquisition with short and long echo spacing for simultaneous quantitative mapping of fat fraction, B0 inhomogeneity, and susceptibility. *Neuroimage*. 2018;172:703-717. doi:10.1016/j.neuroimage.2018.02.012
41. Walsh DO, Gmitro AF, Marcellin MW. Adaptive reconstruction of phased array MR imagery. *Magn Reson Med*. 2000;43(5):682-690. doi:10.1002/(SICI)1522-2594(200005)43:53.0.CO;2-G
42. Liu J, Drangova M. Method for B0 off-resonance mapping by non-iterative correction of phase-errors (B0-NICE). *Magn Reson Med*. 2015;74(4):1177-1188. doi:10.1002/mrm.25497
43. Liu J, Liu T, de Rochefort L, et al. Morphology enabled dipole inversion for quantitative susceptibility mapping using structural consistency between the magnitude image and the susceptibility map. *Neuroimage*. 2012;59(3):2560-2568. doi:10.1016/j.neuroimage.2011.08.082
44. Siepmann J, Siepmann F. Modeling of diffusion controlled drug delivery. *J Control Release*. 2012;161(2):351-362. doi:10.1016/j.jconrel.2011.10.006
45. Prasad M, Dharmatti S, Gokhale S. Magnetic susceptibilities of calcium and strontium ions. *Proc Indian Acad Sci - Section a*. 1945;20(5):224-244. doi:10.1007/BF03046418
46. Charette RS, Melnic CM. Two-stage revision arthroplasty for the treatment of prosthetic joint infection. *Curr Rev Musculoskelet Med*. 2018;11(3):332-340. doi:10.1007/s12178-018-9495-y
47. Alaia EF, Chhabra A, Simpfendorfer CS, et al. MRI nomenclature for musculoskeletal infection. *Skeletal Radiol*. 2021;50(12):2319-2347. doi:10.1007/s00256-021-03807-7
48. Dimov AV, Nguyen TD, Gillen KM, et al. Susceptibility source separation from gradient echo data using magnitude decay modeling. *J Neuroimaging*. 2022;32(5):852-859. doi:10.1111/jon.13014
49. Chen J, Gong NJ, Chaim KT, Otaduy MCG, Liu C. Decompose quantitative susceptibility mapping (QSM) to sub-voxel diamagnetic and paramagnetic components based on gradient-echo MRI data. *Neuroimage*. 2021;242:118477. doi:10.1016/j.neuroimage.2021.118477
50. Shin HG, Lee J, Yun YH, et al. χ-separation: magnetic susceptibility source separation toward iron and myelin mapping in the brain. *Neuroimage*. 2021;240:118371. doi:10.1016/j.neuroimage.2021.118371
51. Emmerich J, Bachert P, Ladd ME, Straub S. On the separation of susceptibility sources in quantitative susceptibility mapping: theory and phantom validation with an in vivo application to multiple sclerosis lesions of different age. *J Magn Reson*. 2021;330:107033. doi:10.1016/j.jmr.2021.107033

52. Putra NE, Leeflang MA, Taheri P, et al. Extrusion-based 3D printing of ex situ-alloyed highly biodegradable MRI-friendly porous iron-manganese scaffolds. *Acta Biomater*. 2021;134:774-790. doi:10.1016/j.actbio.2021.07.042
53. Chen Z, Han Z, Liu G. Repurposing clinical agents for chemical exchange saturation transfer magnetic resonance imaging: current status and future perspectives. *Pharmaceuticals*. 2021;14(1):11. doi:10.3390/ph14010011
54. Gottumukkala RV, Glover MK IV, Yun BJ, et al. Allergic-like contrast reactions in the ED: incidence, management, and impact on patient disposition. *Am J Emerg Med*. 2018;36(5):825-828. doi:10.1016/j.ajem.2017.10.032
55. Sapra A, Bhandari P, Manek M, Gupta S, Sharma S. Fatal anaphylaxis to contrast a reality: a case report. *Cureus*. 2019;11(11):e6214. doi:10.7759/cureus.6214

SUPPORTING INFORMATION

Additional supporting information can be found online in the Supporting Information section at the end of this article.

How to cite this article: Hong G, Khazaee T, Cobos SF, et al. Characterizing diffusion-controlled release of small-molecules using quantitative MRI in view of applications to orthopedic infection. *NMR in Biomedicine*. 2024;37(12):e5254. doi:10.1002/nbm.5254